Environmental Science & Technology

pubs.acs.org/est

Article

Evidence against Rapid Mercury Oxidation in Photochemical Smog

Seth N. Lyman,* Tyler Elgiar, Mae Sexauer Gustin, Sarrah M. Dunham-Cheatham, Liji M. David, and Lei Zhang

Cite This: *Environ. Sci. Technol.* 2022, 56, 11225−11235

Read Online

ACCESS | Metrics & More | Article Recommendations | Supporting Information

ABSTRACT: Mercury pollution is primarily emitted to the atmosphere, and atmospheric transport and chemical processes determine its fate in the environment, but scientific understanding of atmospheric mercury chemistry is clouded in uncertainty. Mercury oxidation by atomic bromine in the Arctic and the upper atmosphere is well established, but less is understood about oxidation pathways in conditions of anthropogenic photochemical smog. Many have observed rapid increases in oxidized mercury under polluted conditions, but it has not been clearly demonstrated that these increases are the result of local mercury oxidation. We measured elemental and oxidized mercury in an area that experienced abundant photochemical activity (ozone >100 ppb) during winter inversion (i.e., cold air pools) conditions that restricted entrainment of air from the oxidized mercury-rich upper atmosphere. Under these conditions, oxidized mercury concentrations decreased day-upon-day, even as ozone and other pollutants increased dramatically. A box model that incorporated rapid kinetics for reactions of elemental mercury with ozone and OH radical overestimated observed oxidized mercury, while incorporation of slower, more widely accepted reaction rates did not. Our results show that rapid gas-phase mercury oxidation by ozone and OH in photochemical smog is unlikely.

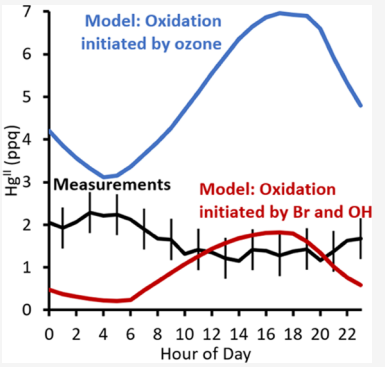

KEYWORDS: *mercury, oxidation, ozone, model, chemical mechanism*

INTRODUCTION

Mercury (Hg) is toxic to humans and wildlife,[1] and anthropogenic activities have enhanced Hg concentrations in all compartments of the environment.[2] Elemental Hg (Hg^0) and many Hg compounds are volatile, and 95% of Hg pollution is emitted to the atmosphere.[3] While concentrations of atmospheric Hg are generally too low to be a direct harm to biota,[4] Hg^0 and oxidized Hg compounds (Hg^{II}) deposit to ecosystems and are methylated in aquatic environments, where they can have a toxic impact.[5] Hg^{II} is more soluble and less volatile than Hg^0, and it is thus efficiently wet- and dry-deposited.[6]

Oxidation of Hg^0 and reduction of Hg^{II} determine much of the atmospheric distribution and eventual ecosystem impacts of Hg pollution.[7−9] Unfortunately, available Hg^{II} measurements are spatially limited, have often been made with flawed instrumentation,[10] and are not able to differentiate among individual chemical species of Hg^{II}.[11] In addition, wall interactions and other challenges have cast doubt on the results of some laboratory kinetics studies.[12,13] These problems have led to uncertainty about which oxidation and reduction reactions are important for atmospheric Hg.

Recent theoretical investigations have provided evidence that oxidation initiated by Br and OH radicals is dominant[9,14] and that gas-phase oxidation initiated by ozone is infeasible.[6] Despite this, several field studies have failed to reconcile Hg^{II} measurements with models that use currently accepted Br and OH chemistry.[7,15,16] Measurements of Hg^{II} collected in polluted environments have often been found to correlate with ozone, and some have asserted that this correlation is due to oxidation of Hg^0 initiated by ozone or other chemical components of photochemical smog.[17] Also, some studies have found a better measurement−model agreement when reactions initiated by ozone or various other pollutants are included.[6] Correlations of Hg^{II} with ozone and other oxidants could instead be due to confounding factors, such as deep convective mixing that entrains Hg^{II}-rich air from the free troposphere, leading to an afternoon increase in both ozone and Hg^{II}.[18,19] On the other hand, measurements in Chinese cities have shown evidence for Hg^0 oxidation under conditions with extremely high concentrations of locally produced particulate matter and little vertical mixing. Chen et al.[20] provided evidence for Hg^0 oxidation on particle surfaces, perhaps by aqueous anions, under these conditions. Heterogeneous Hg^0 oxidation pathways have not been comprehensively explored.[6,21]

We measured atmospheric Hg^0 and Hg^{II} at the Horsepool monitoring station[22] in the Uinta Basin, Utah, during winter

Received: April 5, 2022
Revised: July 12, 2022
Accepted: July 14, 2022
Published: July 25, 2022

and summer 2019 via a method that has been shown to quantitatively capture gas-phase Hg^{II} compounds in ambient air.[23] The Uinta Basin area experiences persistent wintertime temperature inversions (i.e., cold air pools) that trap pollution in a shallow layer close to the surface, which, combined with local emissions from oil and gas activity, allow ozone to form near the surface, sometimes reaching concentrations as high as 140 ppb.[22,24,25] The photochemical mechanisms involved in wintertime ozone formation are similar to those in urban summer, except that low water vapor concentrations during winter limit OH radical production via ozone photolysis. Instead, high concentrations of organic compounds in the atmosphere allow for abundant secondary production of carbonyls, and carbonyl photolysis is the primary radical source.[22] During these events, mixing ratios of compounds and radicals that are known to be involved in atmospheric mercury redox chemistry[9] are in the same range as urban summer ozone.

Winter inversion conditions provide a strong barrier to separate surface-level photochemical pollution from the upper-atmosphere influence.[26] Measurements of Hg in this unique atmospheric condition allowed us to investigate the influence of photochemical smog on Hg^0 oxidation with a reduced confounding effect from entrainment of upper-atmosphere air. Also, particulate matter concentrations in the Uinta Basin are relatively low (an order of magnitude lower than that in the study by Chen et al.; see Figures S1−S3), so we expect any possible confounding influence from heterogeneous Hg^0 oxidation to be relatively low.

METHODS

Site Information. We collected measurements at Horsepool, a measurement station in the central Uinta Basin, Utah. Horsepool is located at latitude 40.143°N, longitude 109.469°W, and 1569 m above sea level. Horsepool is a desert site more than 50 km from any urban development. Many oil and gas wells, as well as other oil and gas infrastructure, are in close proximity to the Horsepool site. Wintertime ozone episodes in the Uinta Basin, and the influence of the regional oil and gas industry on wintertime air quality, have been extensively studied.[24,27−44]

Mercury Measurements. *Dual-Channel System.* We measured Hg^0 and Hg^{II} in ambient air using the dual-channel system described by Lyman et al.[23] The system sampled air through a heated elutriator and impactor that removed particles larger than 2.5 μm, through a 7 m heated perfluoroalkoxy (PFA) Teflon line, and then into one of two channels. One channel pulled air through a pyrolyzer to convert all atmospheric Hg to Hg^0, and the other pulled air through a series of cation-exchange membranes, which retain Hg^{II}, to measure Hg^0. A Tekran 2537B analyzer analyzed the Hg^0 output by both channels, and we calculated Hg^{II} as the difference between the two channels. Poly(tetrafluoroethylene) (PTFE) Teflon valves switched between the two channels at 5 min intervals. Offline processing of the Tekran 2537B detector output, as well as sensitivity improvements to the 2537B, allowed this instrument to achieve a 1 h detection limit for Hg^{II} of 12 ± 2 pg m^{-3} during the winter portion of the study and 17 ± 5 pg m^{-3} for the entire study.

The dual-channel system has been shown to quantitatively collect gas-phase Hg^{II} compounds injected into ambient air.[23] The cation-exchange membranes used in the system to capture Hg^{II} have been shown to collect a wide variety of Hg^{II} compounds[45,46] and do not collect a significant amount of Hg^0.[47,47] While no calibration method exists for particle-phase Hg, we expect that the dual-channel system captures all gas-phase Hg^{II} and Hg^{II} bound to particles smaller than 2.5 μm. Additional information about the dual-channel system is available in Lyman et al.[23]

We used soda lime traps upstream of the 2537B to scrub reactive gases that can passivate the 2537B's gold traps. We replaced soda lime traps and cation-exchange membranes semiweekly. We performed semiweekly injections of Hg^0 from a temperature-controlled saturated Hg^0 vapor source. Hg^0 recovery was 99 ± 2%.

Direct Measurement of Hg Collected on Membranes. As a comparison with the dual-channel method, we collected Hg^{II} on cation-exchange membranes in a separate system, the Reactive Mercury Active System (RMAS). The RMAS used a pump to pull air through two cation-exchange membranes in series at 1 L min^{-1} for 2 weeks periods. The membranes were housed in 47 mm PFA Savillex filter holders. The system collected triplicate samples. After collection, we analyzed the membranes for total Hg content following Luippold et al.[48] The dual-channel system and the RMAS both used identical membranes. Luippold et al.[48] provide more detail about the RMAS.

We also collected Hg^{II} in triplicate on nylon membranes (two in series) with the RMAS. After collection, we sequentially thermally desorbed the nylon membranes into a Tekran 2537 Hg^0 analyzer and compared thermal desorption profiles from samples against standard profiles to make inferences about Hg^{II} speciation.[46,48] Hg^{II} speciation inferred by this method has been shown to be generally consistent with expected Hg^0 oxidant distribution in previous studies,[48,49] though thermal desorption reference standards are limited to commercially available Hg^{II} compounds, and many predicted products of Hg^0 oxidation (e.g., BrHgOH, $HgOH_2$, BrHgO-NO, HgBrCl[9,50]) are not commercially available, so inferences of speciation may not be exact.

Other Measurements. We pulled air through a PTFE filter and a PFA manifold at 10 L min^{-1} for trace gas measurements. We measured ozone, NO_x, NO_y, and CO with Ecotech 9810, 9841, 9843, and 9830 analyzers, respectively. We measured methane and total nonmethane hydrocarbons with a Chromatotec ChromaTHC analyzer and $PM_{2.5}$ with a Met One BAM 1020. We performed maintenance at intervals as recommended by instrument manufacturers, including regular checks of the BAM 1020 flow rate and annual checks of its detector and reference membrane. We calibrated all gas-phase measurements weekly with an Ecotech GasCal dynamic dilution calibrator, which used diluent gas generated by a Thermo 701H zero air generator and certified compressed gas standards. We calibrated NO_y and NO_2 via gas-phase titration with the GasCal calibrator. We checked the GasCal ozone calibration at the beginning and end of the measurement season with a NIST-traceable reference standard. We only used trace gas data for analysis that had calibration span checks within 5% of expected values.

We measured speciated nonmethane organic compounds, including C2−C10 hydrocarbons, C1−C3 alcohols, and a suite of 13 carbonyls, as described by Lyman et al.[51] We collected air in silonite-coated whole-air canisters for hydrocarbon and alcohol analysis and on 2,4-dinitrophenylhydrazine (DNPH) cartridges for carbonyl analysis. We collected one 3 h sample daily, alternating between start times of midnight and noon.

https://doi.org/10.1021/acs.est.2c02224
Environ. Sci. Technol. 2022, 56, 11225−11235

We preconcentrated gases of interest from canisters in the laboratory via a cold-trap dehydration method on an Entech 7200 and analyzed them by gas chromatography−flame-ionization detection (C1−C3 hydrocarbons) and gas chromatography−mass spectrometry (remaining compounds) with a Shimadzu QP-2010. Quality assurance information was provided by Lyman et al.[51]

We measured snow depth (MaxBotix MB7092), incoming and outgoing visible radiation (Kipp and Zonen CNR4), wind speed and direction (RM Young 05108-45-L), temperature and relative humidity (Vaisala HMP155), and barometric pressure (Vaisala PTB101B), and recorded measurements from these and the instruments mentioned above with a Campbell CR1000 datalogger. We checked all meteorological instrumentation against NIST-traceable standards annually.

Delineation of Inversion Episodes. Vertical measurements of the atmospheric structure are not collected routinely in the Uinta Basin. As an alternative, Mansfield[31] developed a "pseudo-lapse rate" for the Basin, which is the change in temperature with altitude at surface meteorological stations. The pseudo-lapse rate provides a relative measure of inversion intensity. We considered all days with a daytime pseudo-lapse rate of −5 °C km^{-1} or less to be inversion days.

HYSPLIT Back Trajectories. We computed air mass back trajectories using the HYSPLIT Lagrangian trajectory model.[52] We used the NAM 12 km forecast data archive as input for the model. The NAM 12 km data set and other meteorological data sets were unable to simulate winter inversion conditions in the Uinta Basin during 2019, and we thus did not compute trajectories for winter conditions. Failure to simulate cold pool conditions in complex terrain is a common problem for mesoscale meteorological models.[30]

We computed daily 7 days back trajectories for the summertime measurement period, with each trajectory terminating at 200 m above the study site at 14:00 local standard time (the average time of the highest daily Hg^{II}). We used the HYSPLIT model's ensemble mode with default settings to compute 27 trajectories for each start time. Each of the ensemble trajectories used starting meteorological data that were offset in different directions from the actual starting point to characterize the uncertainty associated with the meteorological input data. Trajectory statistics reported above are for all trajectories in each ensemble.

Box Model. We used the Framework for 0-D Atmospheric Modeling (F0AM) box model[53] version 4.1, using a variation of the diel cycle example setup, for the winter and summer simulations. We used average hourly meteorological data over each 4-day modeled episode as input for each modeled day. We averaged all measured ozone precursor gases (NO, NO_2, CO, methane, hydrocarbons, alcohols, and carbonyls) over the study period and forced the model to keep their concentrations constant throughout the study period. We used family conservation for NO_x, which kept NO_x concentrations constant but allowed NO and NO_2 to vary as modeled. For winter, we used an albedo of 0.7, consistent with measurements over the study period, and an ozone column of 275 Dobson units (from OMI satellite data (OMDOAO3e v003) obtained from the National Aeronautics and Space Administration's Giovanni application[54]). We used the same time-varying boundary layer heights and dilution constants used by Edwards et al.[22]

Use of the average concentration of individual nonmethane organics led to overestimation of ozone production, so we scaled each compound to 75% of its average over the study period. Daytime concentrations of organics were higher than nighttime during the study period (the opposite pattern is usually true at the Horsepool station).[37] Nighttime concentrations at the site were roughly equivalent to the 75% scaled values.

We assumed halogen radical concentrations were low (Cl = 0 ppq,[55] Br = 2 ppq[56]). Halogen radical concentrations can be higher than this in instances with strong influence from the free troposphere,[57] but we assumed that the upper-atmosphere influence was limited during the model period. We used the halogen chemical mechanism of Sherwen et al.[58] available with F0AM.

We held Hg^0 constant at 168 ppq (1.50 ng m^{-3}) throughout the simulation and included a starting Hg^{II} concentration of 6 ppq (55 pg m^{-3}), consistent with measurements at the beginning of the study period. We used a background ozone concentration of 50 ppb[22] and a background Hg^{II} concentration of 4 ppq (35 pg m^{-3}).

For basic photochemistry, we used a subset of the reactions from the Master Chemical Mechanism (MCM) version 3.3.1[59,60] that involve each of the measured organic compounds. We also coded Hg^0 oxidation reactions listed by Pal and Ariya,[61] Ye et al.,[16] Travnikov et al.,[7] and Shah et al.[9] into F0AM format and included them in separate model runs. For the Shah et al. mechanism, initial and background Hg^{II} was assumed to be $HgBr_2$. Since the other mechanisms did not include Hg^{II} reduction reactions, initial, background, and product Hg^{II} was coded as generic Hg^{II}, rather than a specific compound. We scaled photolysis rate constants in the Shah et al. mechanism to model values for NO_2 photolysis.

We calculated dry deposition of Hg^{II} as described by Zhang et al.,[62] as applied by Lyman et al.[63] We used average meteorological conditions during the modeled periods to determine a constant deposition velocity. We used land use category 10 and assumed a leaf area index of 0.3, snow depth of 27 cm (for winter), molecular diffusivity of 0.06 cm^2 s^{-1}, mesophyll resistance of 0 s m^{-1}, and $\alpha = \beta = 2$. We also performed a model sensitivity study with $\alpha = \beta = 10$, which is assumed to be similar to nitric acid, which led to an increase in the wintertime deposition velocity from 0.14 to 0.22 cm s^{-1}.

For the summertime model, we used boundary layer heights extracted from the high resolution rapid refresh (HRRR) data set.[64] We forced ozone in the summertime model to match observed average values, and we set the dilution constant to allow for complete dilution over each 24-h period (1/86 400 s). We used the same dry deposition model to calculate a summertime deposition velocity of 0.11 cm s^{-1}.

GEOS-Chem Model. We used the GEOS-Chem global 3D chemical transport model (v12.9.0) driven with assimilated meteorological data implementing the Hg chemistry used by Shah et al.[9] The global GEOS-Chem simulations were made at 2° × 2.5° resolution using Goddard Earth Observing System-Forward Processing (GEOS-FP) meteorology to generate temporally varying boundary conditions for Hg species; for higher-resolution nested simulations at 0.25° × 0.3125° over the contiguous U.S., GEOS-Chem has a fully coupled NO_x-O_x-hydrocarbon-aerosol chemistry in the troposphere and stratosphere. The Hg simulation uses the monthly oxidant and aerosol concentrations archived from the full chemistry simulation. The anthropogenic Hg emissions are from Streets et al.[65] Shah et al. detail the chemistry and other emissions used for Hg simulations.

https://doi.org/10.1021/acs.est.2c02224
Environ. Sci. Technol. 2022, 56, 11225−11235

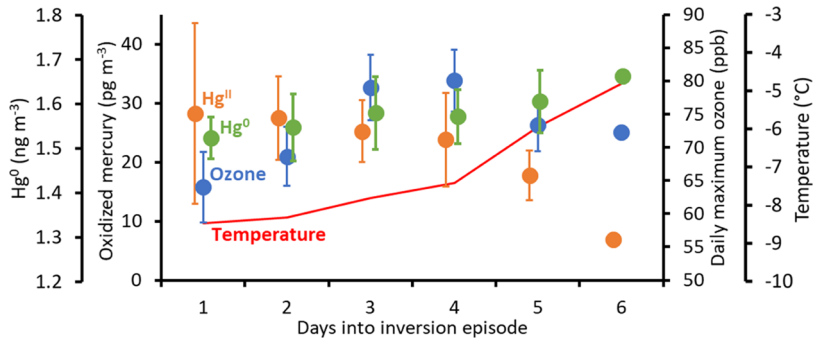

Figure 1. Average daily Hg^0, Hg^{II}, and temperature, along with daily maximum 1 h average ozone, on the first 6 days of winter inversion episodes that occurred during 2019. Whiskers represent 95% confidence intervals. To better show trends, Hg^0, Hg^{II}, and ozone were normalized using day 4 values. n = 5 for days 1−4, n = 4 for day 5, and n = 2 for day 6. Figures S1−S3 show a time series of the episodes used to create this figure.

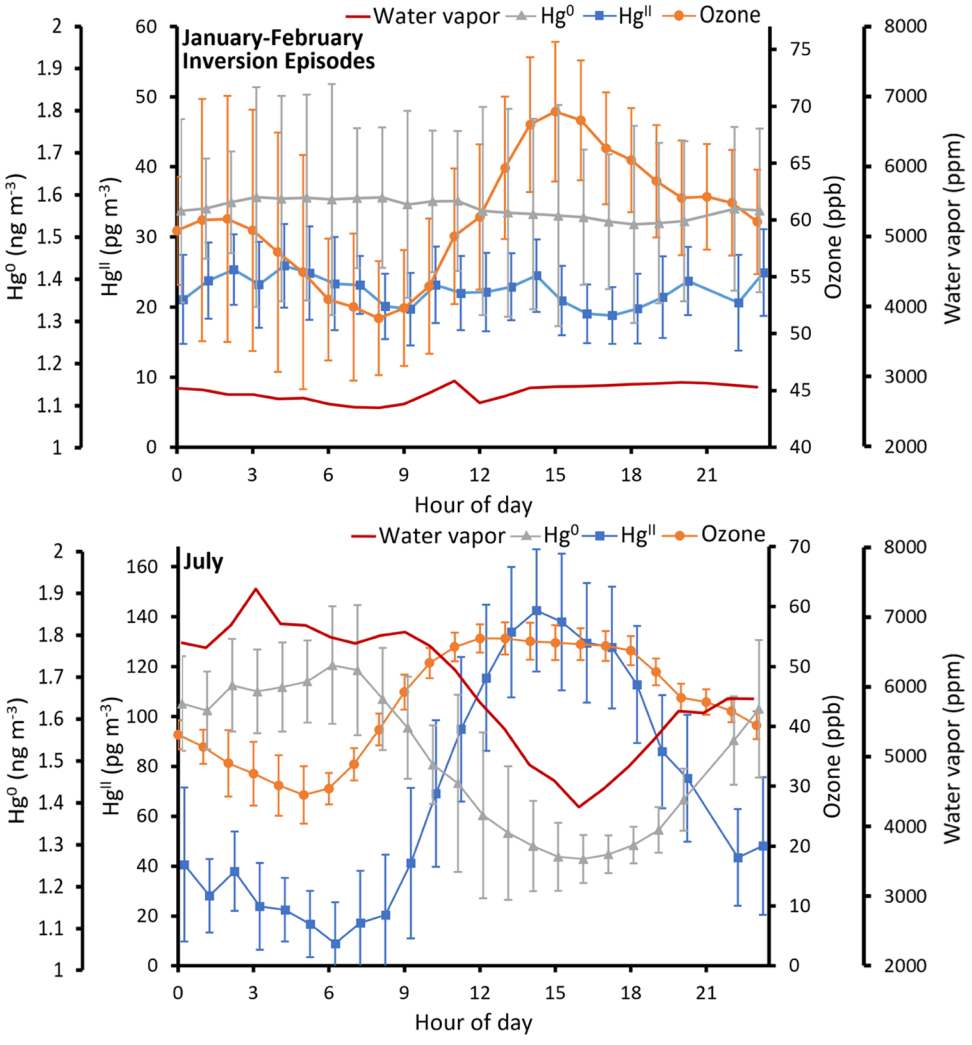

Figure 2. Diel profiles of Hg^0, Hg^{II}, ozone, and water vapor (calculated from temperature, relative humidity, and pressure) during the wintertime inversion episodes shown in Figure 1 (top panel) and during July 2019 (bottom panel). *Y*-axis scales are different for each panel. Lines indicate means, and whiskers show 95% confidence intervals.

RESULTS AND DISCUSSION

Winter Inversion Episodes. Snow cover persisted throughout the Uinta Basin from January through early March 2019, leading to several episodes with multiday temperature inversions and maximum ozone of 102 ppb (Figures S1 and S3). Figure 1 shows daily average ozone, Hg^0, and Hg^{II} over each inversion day during five 2019 episodes. It shows that ozone increased day-upon-day for the first several days of each episode before leveling off, as has been observed by others during similar episodes.[22,24] Concentrations of other pollutants, including carbon monoxide, methane, and particulate matter with an aerodynamic diameter smaller than 2.5 μm ($PM_{2.5}$), increased day-upon-day as locally emitted pollution was trapped under the inversion layer (Figures S1−

https://doi.org/10.1021/acs.est.2c02224
Environ. Sci. Technol. 2022, 56, 11225−11235

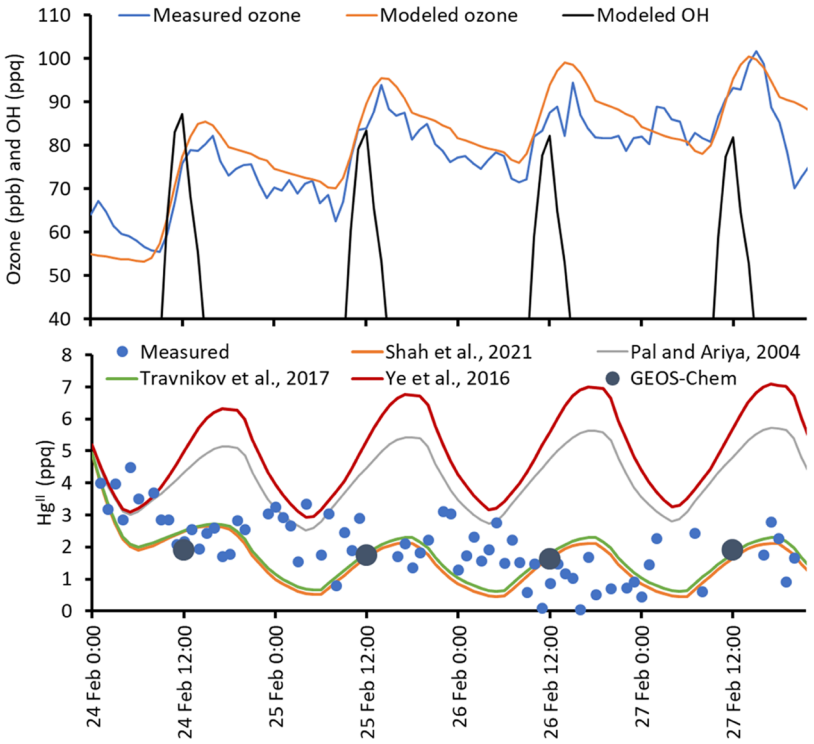

Figure 3. Box model and GEOS-Chem model results for 24−27 February 2019. Measured ozone and modeled ozone and OH radical are shown in the top panel. Measured Hg^{II} and Hg^{II} modeled with four different chemical mechanisms in F0AM are shown in the bottom panel, along with daily average values from GEOS-Chem.

S3). Hg^0 also increased day-upon-day ($p = 0.02$ for significance of slope), indicating the presence of local Hg^0 sources (see Supporting Information for more information about possible sources).

In contrast, Hg^{II} concentrations tended to decrease during inversion episodes ($p < 0.01$; Figure 1). This implies that local Hg^{II} emissions were less than Hg^{II} loss processes (which could include deposition to the snow, reduction to Hg^0, or mixing out of the inversion layer). It also implies that oxidation of Hg^0 to Hg^{II} was slower than these same loss processes, despite photochemistry sufficient to produce ozone exceeding 100 ppb.

Summertime Hg^{II}. Figure 2 shows a diel plot of Hg^0, Hg^{II}, and ozone at the Horsepool station during winter and summer 2019. Hg^{II} did not exhibit statistically significant ($p = 0.27$) diel variation during winter and was weakly negatively correlated with ozone (Pearson $r = -0.35$; $p < 0.01$), but during summer, Hg^{II} followed a clear diel pattern, with higher concentrations in the afternoon and a positive correlation with ozone (Pearson $r = 0.63$; $p < 0.01$). Summertime ozone at Horsepool was within the range of background ozone in the region.[66,67] More discussion about Figure 2 is available in the Supporting Information.

Our finding that summertime ozone and Hg^{II} were correlated is not new and has been reported by many others at sites around the world (e.g., Mao et al.[17]). Many of these studies have asserted that this correlation is evidence that ozone and/or other components of photochemical smog oxidized Hg^0 to Hg^{II}.[68−71] Instead, we found evidence that the measurement station was strongly influenced by upper-atmosphere air on days with high Hg^{II} during summer.

Air measured on the 10% of summer days with the highest Hg^{II} was associated with air mass back trajectories that had lower average latitude ($p < 0.01$), lower relative humidity ($p < 0.01$), and that were less likely to have experienced rainfall ($p < 0.01$) than the 10% of summertime days with the lowest Hg^{II}. Figures S4 and S5 show example trajectories. Also, surface temperature ($p < 0.01$) and solar radiation ($p < 0.01$) were higher, while relative humidity ($p < 0.01$) and daytime carbon monoxide concentrations ($p = 0.01$) were lower, on days with the highest Hg^{II}. Together, these pieces of evidence show that, during summer, air containing high Hg^{II} likely descended from the free troposphere, which is rich in both Hg^{II} and ozone[72] and tends to be drier and poorer in carbon monoxide.[73] Thus, the correlation of high summertime Hg^{II} with ozone is likely due to a common air mass source region, rather than local oxidation of Hg^{0-} by ozone or associated pollutants.[18] This could also be true in urban areas with summertime photochemical smog, where both photochemistry and deep convective mixing that entrains Hg^{II}-rich air from aloft can occur simultaneously.

Winter Box Model Results. We used the F0AM box model[53] to compare our measurements against expected Hg^{II} production and loss with several proposed gas-phase Hg chemical mechanisms. Simulated and measured ozone agreed well ($r^2 = 0.79$; root mean square error = 6.4 ppb), and OH radical production was similar to expected values (23.6 ppb day^{-1}, compared to 18.5 ppb day^{-1} for similar conditions by Edwards et al.[22]).

Chemical mechanisms that included relatively fast rates for the reaction of ozone and OH radical with Hg^0 overproduced Hg^{II}. Pal and Ariya's[61] reaction rate of ozone with Hg^0 (3.5×10^{-19} cm^3 $molecule^{-1}$ s^{-1} for average F0AM model conditions), which has been discredited by others as too fast,[74] led to 250 ± 113% more Hg^{II} than hourly measurements on the fourth modeled day (Figure 3). A mechanism used by

https://doi.org/10.1021/acs.est.2c02224
Environ. Sci. Technol. 2022, 56, 11225−11235

Ye et al.[16] that included reactions of Hg^0 with ozone (4.3×10^{-19} cm^3 $molecule^{-1}$ s^{-1} for model conditions) and OH (1.1×10^{-13} cm^3 $molecule^{-1}$ s^{-1} for model conditions) overpredicted by 295 ± 139% on the fourth modeled day. By contrast, the Shah et al.[9] mechanism, which included initial oxidation of Hg^0 by OH (9.1×10^{-14} cm^3 $molecule^{-1}$ s^{-1} for the initial OH−Hg^0 reaction in model conditions), Br, and Cl, and a mechanism used by Travnikov et al.[7] (reaction rates of 3.0×10^{-20} and 3.0×10^{-14} cm^3 $molecule^{-1}$ s^{-1} for ozone and OH, respectively), reproduced measured Hg^{II} on the fourth modeled day within the range of uncertainty (percent differences of 98 ± 27 and 113 ± 31%, respectively).

The measurements conducted for this study were inadequate to determine exactly which oxidation reactions exist and are dominant in ambient air, but they correspond better with the relatively slow gas-phase Hg^0 oxidation of the Shah et al. and Travnikov et al. mechanisms, providing evidence against rapid oxidation of Hg^0 in the presence of typical photochemical pollutants.

Hg^0 oxidation during polluted winter inversion episodes was too slow to allow for large diurnal variability in measured Hg^{II} or in modeled Hg^{II} for the Shah et al. mechanism. Indeed, for the Shah et al. mechanism, most (83%) of the Hg^{II} present on the fourth model day was due to entrainment from above the boundary layer, even with the limited vertical mixing used for the inverted conditions. Eighty-eight percent of Hg^{II} on the fourth modeled day in the Shah et al. mechanism was $HgBr_2$. Almost all of this $HgBr_2$ was due to entrainment from above the boundary layer. When we set exchange from above the boundary layer to zero, 58% of modeled Hg^{II} was comprised of compounds that were generated by the initial oxidation of Hg^0 by OH radical. The remainder was nearly all HgBrOH.

Photolysis of Hg^I and Hg^{II} compounds had a small impact on Hg^{II} mixing ratios, probably because the reaction of dominant Hg^I compounds with ozone was faster than photolysis.[9] Without photolysis reactions, Hg^{II} in the Shah et al. model was 5 ± 1% higher. Increasing photolysis rate constants by 10 times led to 9% lower Hg^{II}.

Modeled Hg^{II} loss in the F0AM model was due to dry deposition. We used a dry deposition rate of 0.14 cm s^{-1}, which we calculated from the model of Zhang et al.[62] We also performed a sensitivity test in which we assumed Hg^{II} deposited as readily as nitric acid (see the Methods section for details), which led to an average dry deposition rate of 0.22 cm s^{-1}. Hg^{II} on the fourth modeled day was only 70% high with the increased deposition rate. Without any dry deposition, the Shah et al. mechanism produced 4.7 times more Hg^{II} by the fourth modeled day.

During winter inversion episodes, measured Hg^{II} tended to be slightly lower during the day, while all of the model mechanisms produced the opposite trend (Figure 3, TOC art). In the model (and, almost certainly, in reality), exchange with air above the boundary layer was faster during daytime, and local Hg^{II} production depended on the presence of daytime radical species. The model included a uniform dry deposition rate for all hours of the day, while the actual rate was likely higher in the day when wind turbulence was higher and temperatures were warmer. This could have dampened the daytime Hg^{II} increase or even led to a daytime decrease in Hg^{II}. Alternatively, nighttime Hg^{II} production via a mechanism not included in the model could have led to higher Hg^{II} during the night.

Summer Box Model Results. We also modeled a summertime high Hg^{II} episode (25−28 June 2019; maximum daytime Hg^{II} of 254 pg m^{-3}). When vertical mixing in the model was turned off to separate local Hg^{II} production from Hg^{II} entrained from above the boundary layer, maximum Hg^{II} on the fourth modeled day was only 1.3 ppq (12 pg m^{-3}) for the Shah et al. mechanism but was 15.4 ppq (137 pg m^{-3}) for the Ye et al. mechanism. As described above, however, high Hg^{II} episodes in summer were associated with evidence of strong free tropospheric influence (including, during this specific episode, Hg^0 of 1.0 ng m^{-3}, carbon monoxide of 80 ppb, and relative humidity of 7% during afternoon hours). While the Ye et al. mechanism produced high Hg^{II} during summer, we submit that this and other similar mechanisms are unlikely to represent reality. When we used the Shah et al. mechanism with vertical mixing, an Hg^{II} concentration of 38 ppq (340 pg m^{-3}) in the free troposphere was required for modeled Hg^{II} to match measurements. This free troposphere Hg^{II} concentration is consistent with elevated Hg^{II} plumes observed in the free troposphere by aircraft.[57,75] Figure 4 summarizes Hg^{II} concentrations, as well as processes that increased and decreased Hg^{II} in the modeled boundary layer, for the wintertime and summertime models.

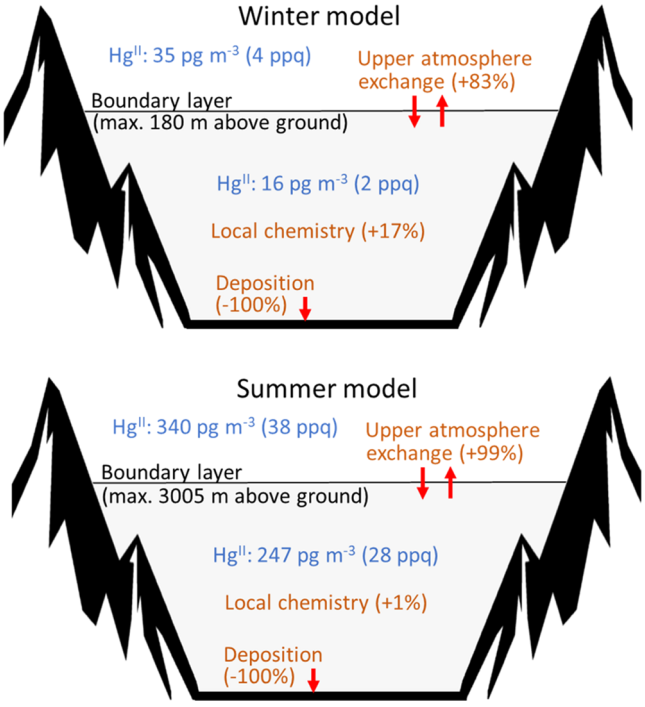

Figure 4. Summary of winter and summer box model results with Shah et al. chemistry. Hg^{II} concentrations are shown in blue (boundary layer concentrations are maxima on the fourth modeled day), and processes that increase and decrease boundary layer Hg^{II} are shown in orange.

GEOS-Chem Model Results. Concentrations of Hg^{II} simulated with the GEOS-Chem global chemical transport model,[9] which uses a chemical mechanism very similar to that of Shah et al., were within the range of our wintertime measurement results (Figure 3). The coarse horizontal resolution of the GEOS-Chem simulation (0.25° × 0.3125° over the contiguous U.S.) did not allow for capture of local temperature inversion conditions, so its simulations represent

https://doi.org/10.1021/acs.est.2c02224
Environ. Sci. Technol. 2022, 56, 11225−11235

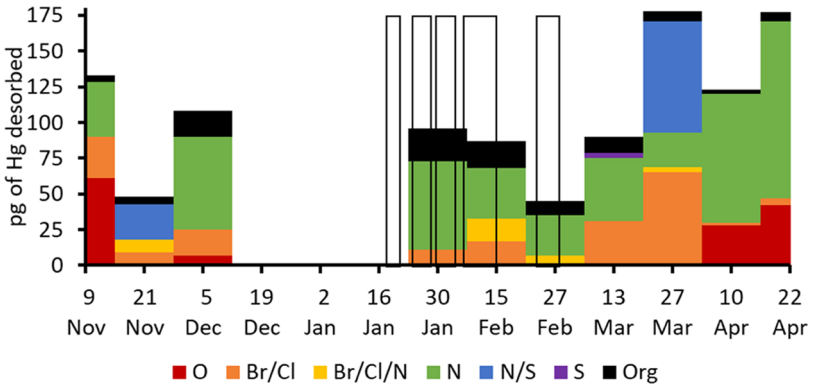

Figure 5. Fraction of Hg^{II} desorbed from nylon membranes that was consistent with desorption of Hg^{II} emitted from permeation tubes containing HgO (O in the figure), $HgBr_2$ (Br) and $HgCl_2$ (Cl), $Hg(NO_3)_2$ (N), $HgSO_4$ (S), and CH_3HgCl (Org). The empty boxes show periods during which multiday inversion conditions occurred.

regional surface-level Hg^{II} in the absence of pollution buildup under the inversion. This provides further evidence that rapid local oxidation is not needed to explain our Hg^{II} measurements. Additional results from the GEOS-Chem model are available in the Supporting Information.

Direct Analysis of Hg^{II} Collected on Membranes. We collected 2-week samples of ambient Hg^{II} on cation-exchange and nylon membranes using the RMAS measurement system[48] and thermally desorbed Hg from the nylon membranes in the laboratory to infer Hg^{II} speciation. Consistent with results from the dual-channel instrument, RMAS cation-exchange membranes recovered lower Hg^{II} during collection periods that encompassed winter inversion episodes with local ozone production than during other periods (30 ± 14 versus 57 ± 18 pg m^{-3}). Hg recovered from RMAS membranes correlated well with dual-channel Hg^{II} ($r^2 = 0.99$; $p < 0.01$), but the dual-channel system recovered less Hg^{II} (dual channel:RMAS slope = 0.68; Figure S12). The RMAS had no apparatus to remove particles, allowing it to collect all particle-bound Hg^{II}, which may explain at least some of the difference between the two systems. It is also possible that some Hg^{II} compounds degraded while traveling through the 7 m heated inlet line of the dual-channel system, in contrast to the inletless RMAS. Gustin et al.[76] found that recovery of $HgBr_2$ decreased with distance along a PFA manifold and concluded that this was caused by the reduction of $HgBr_2$ to Hg^0 within the manifold. Lyman et al.[23] showed quantitative recovery of $HgBr_2$ and $HgCl_2$ with the dual-channel system used in this study, but it is possible that the reduction of other ambient Hg^{II} compounds occurred or that other chemical reactions occurred within the inlet line.[77]

Thermal desorption results of Hg^{II} speciation obtained during winter 2018−2019 are shown in Figure 5. While sample Hg^{II} consistent with oxygen-containing compounds made up an average of 18% of total Hg^{II} during sampling periods without inversion conditions, none was observed during sampling periods that included inversions. This may indicate that, consistent with findings from the box model, Hg^0 oxidation by O-containing oxidants was low during inversion episodes.

Figure 5 shows thermal desorption-based Hg^{II} speciation for winter 2019. In the Shah et al. model run, most Hg^{II} on the fourth modeled day was due to entrainment from above the inverted layer, so we expect local sources and local oxidants had relatively low influence on Hg^{II} speciation. The majority of sample Hg^{II} desorbed was consistent with Hg^{II} emitted from $Hg(NO_3)_2$-containing permeation tubes, similar to the findings of Luippold et al. for our measurement site.[78] Nitrate radical, which is common in photochemical smog during night, may react with Hg^I compounds, as has been proposed by Peleg et al.,[79] but likely does not oxidize Hg^0.[80,8180,81] Modeled wintertime nitrate radical concentrations were low (maximum of 2.4 ppt). We expect that Hg^{II} consistent with $HgCl_2$ and $HgBr_2$ originated in the free troposphere.[49] Oxidation mechanisms for the organic and sulfur-containing Hg^{II} compounds shown in the figure are unknown. Organic compound concentrations were high during winter inversion periods (average 896 ppb C of total nonmethane organics during the modeled inversion episode), and previous work has shown that a large fraction of $PM_{2.5}$ mass in the Uinta Basin is organic.[55] While the model indicated that the majority of Hg^{II} during inversion episodes originated outside the inverted layer, the thermal desorption results suggest that some local Hg^{II} production may have occurred.

Applicability. This work indicates that rapid gas-phase oxidation of Hg^0 during photochemical smog events is unlikely to lead to high Hg^{II} at the surface, though we concede that exceptions may exist, especially in cases with high concentrations of halogens or in cases dominated by heterogeneous chemistry. Peng et al.,[82] for example, found high concentrations of reactive halogens in air polluted by coal burning in China, which likely led to rapid, local Hg^0 oxidation. Also, as discussed in the introduction, evidence for rapid Hg^0 oxidation exists for some extreme particle pollution events.[20] The source of high nighttime Hg^{II} in Jerusalem, Israel, is also uncertain and may be due to rapid, local oxidation, though the oxidants responsible are unknown.[83] All of these cases, however, involve either unusually high concentrations of known Hg^0 oxidants or the possibility of new, unexplored oxidation mechanisms. In this study, Hg^0 oxidation occurred too slowly, and deposition too quickly, for gas-phase reactions to lead to large daily increases in Hg^{II} at the surface, even during an intense photochemical smog event with high ozone concentrations.

■ ASSOCIATED CONTENT

Supporting Information

The Supporting Information is available free of charge at https://pubs.acs.org/doi/10.1021/acs.est.2c02224.

Time series of all available data (Figures S1−S3), additional discussion about possible local sources of Hg^0,

https://doi.org/10.1021/acs.est.2c02224
Environ. Sci. Technol. 2022, 56, 11225−11235

explanation of features in Figure 2, example air mass back trajectories (Figures S4 and S5), additional GEOS-Chem model results (Figures S6−S11), and additional RMAS membrane sampling system results (Figure S12) (PDF)

AUTHOR INFORMATION

Corresponding Author

Seth N. Lyman − *Bingham Research Center, Utah State University, Vernal, Utah 84078, United States; Department of Chemistry and Biochemistry, Utah State University, Logan, Utah 84322, United States;* orcid.org/0000-0001-8493-9522; Email: seth.lyman@usu.edu

Authors

Tyler Elgiar − *Bingham Research Center, Utah State University, Vernal, Utah 84078, United States*

Mae Sexauer Gustin − *Department of Natural Resources and Environmental Science, University of Nevada, Reno, Reno, Nevada 89557, United States;* orcid.org/0000-0002-9306-2037

Sarrah M. Dunham-Cheatham − *Department of Natural Resources and Environmental Science, University of Nevada, Reno, Reno, Nevada 89557, United States*

Liji M. David − *Bingham Research Center, Utah State University, Vernal, Utah 84078, United States;* orcid.org/0000-0002-0099-7715

Lei Zhang − *School of the Environment, Nanjing University, Nanjing, Jiangsu 210023, China;* orcid.org/0000-0003-2796-6043

Complete contact information is available at: https://pubs.acs.org/10.1021/acs.est.2c02224

Author Contributions

S.N.L. designed and oversaw most aspects of the study. T.E. and S.N.L. collected data and maintained instrumentation at the field site and contributed equally to data analysis. S.M.D.-C. and M.S.G. oversaw the RMAS measurements and conducted laboratory analysis of membranes. S.N.L. conducted the box modeling exercises. L.M.D. conducted the GEOS-Chem modeling. L.Z. analyzed nylon membrane thermal desorption results. S.N.L. prepared the original draft of the manuscript, and all authors contributed to review and editing of the manuscript.

Notes

The authors declare no competing financial interest.

Dual-channel Hg data and other chemical and meteorological data measured at Horsepool are available.[84] Other data, including RMAS membrane data and model input and output files, are available from the corresponding author upon request.

ACKNOWLEDGMENTS

This project was primarily funded by the United States National Science Foundation grants 1700722, 1700711, and 1951513. Funding to conduct the nonmercury measurements at the Horsepool station was provided by the Uintah Impact Mitigation Special Service District and the Utah Legislature. Makenzie Holmes and Trevor O'Neil at Utah State University analyzed the whole-air canister and DNPH cartridge samples collected at the site, and Trevor O'Neil assisted with site maintenance. Randy Anderson at Utah State University assisted with the development of the dual-channel instrument. Many components of the dual-channel instrument were loaned by Dan Jaffe at the University of Washington. The authors thank Carrie Womack of the U.S. National Oceanic and Atmospheric Administration Chemical Sciences Laboratory for generously donating her time to help us with the F0AM model. The authors thank Ted Dibble of the State University of New York College of Environmental Science and Forestry for reviewing the manuscript and Viral Shah of Harvard University for help with the implementation of the GEOS-Chem model.

REFERENCES

(1) Rice, K. M.; Walker, E. M., Jr.; Wu, M.; Gillette, C.; Blough, E. R. Environmental mercury and its toxic effects. *J. Prevent. Med. Public Health* **2014**, *47*, 74.

(2) Amos, H. M.; Sonke, J. E.; Obrist, D.; Robins, N.; Hagan, N.; Horowitz, H. M.; Mason, R. P.; Witt, M.; Hedgecock, I. M.; Corbitt, E. S.; Sunderland, E. M. Observational and modeling constraints on global anthropogenic enrichment of mercury. *Environ. Sci. Technol.* **2015**, *49*, 4036−4047.

(3) Selin, N. E. Global Biogeochemical Cycling of Mercury: A Review. *Annu. Rev. Environ. Resour.* **2009**, *34*, 43−63.

(4) Broussard, L. A.; Hammett-Stabler, C. A.; Winecker, R. E.; Ropero-Miller, J. D. The toxicology of mercury. *Lab. Med.* **2002**, *33*, 614−625.

(5) Obrist, D.; Kirk, J. L.; Zhang, L.; Sunderland, E. M.; Jiskra, M.; Selin, N. E. A review of global environmental mercury processes in response to human and natural perturbations: Changes of emissions, climate, and land use. *Ambio* **2018**, *47*, 116−140.

(6) Lyman, S. N.; Cheng, I.; Gratz, L. E.; Weiss-Penzias, P.; Zhang, L. An updated review of atmospheric mercury. *Sci. Total Environ.* **2020**, *707*, No. 135575.

(7) Travnikov, O.; Angot, H.; Artaxo, P.; Bencardino, M.; Bieser, J.; D'Amore, F.; Dastoor, A.; De Simone, F.; DIéguez, M. C.; Dommergue, A.; Ebinghaus, R.; Feng, X. B.; Gencarelli, C. N.; Hedgecock, I. M.; Magand, O.; Martin, L.; Matthias, V.; Mashyanov, N.; Pirrone, N.; Ramachandran, R.; Read, K. A.; Ryjkov, A.; Selin, N. E.; Sena, F.; Song, S.; Sprovieri, F.; Wip, D.; Wangberg, I.; Yang, X. Multi-model study of mercury dispersion in the atmosphere: atmospheric processes and model evaluation. *Atmos. Chem. Phys.* **2017**, *17*, 5271−5295.

(8) Saiz-Lopez, A.; Sitkiewicz, S. P.; Roca-Sanjuán, D.; Oliva-Enrich, J. M.; Dávalos, J. Z.; Notario, R.; Jiskra, M.; Xu, Y.; Wang, F.; Thackray, C. P.; Sunderland, E. M.; Jacob, D. J.; Travnikov, O.; Cuevas, C. A.; Acuña, A. U.; Rivero, D.; Plane, J. M. C.; Kinnison, D. E.; Sonke, J. E. Photoreduction of gaseous oxidized mercury changes global atmospheric mercury speciation, transport and deposition. *Nat. Commun.* **2018**, *9*, No. 4796.

(9) Shah, V.; Jacob, D. J.; Thackray, C. P.; Wang, X.; Sunderland, E. M.; Dibble, T. S.; Saiz-Lopez, A.; Černušák, I.; Kellö, V.; Castro, P. J.; et al. Improved mechanistic model of the atmospheric redox chemistry of mercury. *Environ. Sci. Technol.* **2021**, *55*, 14445−14456.

(10) Cheng, I.; Zhang, L. Uncertainty assessment of gaseous oxidized mercury measurements collected by Atmospheric Mercury Network. *Environ. Sci. Technol.* **2017**, *51*, 855−862.

(11) Khalizov, A. F.; Guzman, F. J.; Cooper, M.; Mao, N.; Antley, J.; Bozzelli, J. Direct detection of gas-phase mercuric chloride by ion drift-Chemical ionization mass spectrometry. *Atmos. Environ.* **2020**, *238*, No. 117687.

(12) Goodsite, M. E.; Plane, J.; Skov, H. A theoretical study of the oxidation of Hg0 to HgBr2 in the troposphere. *Environ. Sci. Technol.* **2004**, *38*, 1772−1776.

(13) Saiz-Lopez, A.; Travnikov, O.; Sonke, J. E.; Thackray, C. P.; Jacob, D. J.; Carmona-García, J.; Francés-Monerris, A.; Roca-Sanjuán, D.; Acuña, A. U.; Dávalos, J. Z.; et al. Photochemistry of oxidized Hg (I) and Hg (II) species suggests missing mercury oxidation in the troposphere. *Proc. Natl. Acad. Sci. U.S.A.* **2020**, *117*, 30949−30956.

(14) Dibble, T. S.; Tetu, H. L.; Jiao, Y.; Thackray, C. P.; Jacob, D. J. Modeling the OH-Initiated Oxidation of Mercury in the Global

Atmosphere Without Violating Physical Laws. *J. Phys. Chem. A* **2020**, *124*, 444−453.
(15) Weiss-Penzias, P.; Amos, H.; Selin, N.; Gustin, M.; Jaffe, D.; Obrist, D.; Sheu, G.-R.; Giang, A. Use of a global model to understand speciated atmospheric mercury observations at five high-elevation sites. *Atmos. Chem. Phys.* **2015**, *15*, 1161−1173.
(16) Ye, Z.; Mao, H.; Lin, C. J.; Youn Kim, S. Investigation of processes controlling summertime gaseous elemental mercury oxidation at midlatitudinal marine, coastal, and inland sites. *Atmos. Chem. Phys.* **2016**, *16*, 8461−8478.
(17) Mao, H.; Cheng, I.; Zhang, L. Current understanding of the driving mechanisms for spatiotemporal variations of atmospheric speciated mercury: A review. *Atmos. Chem. Phys.* **2016**, *16*, 12897−12924.
(18) Weiss-Penzias, P.; Gustin, M. S.; Lyman, S. N. Observations of speciated atmospheric mercury at three sites in Nevada: Evidence for a free tropospheric source of reactive gaseous mercury. *J. Geophys. Res.* **2009**, *114*, No. D14302.
(19) Shah, V.; Jaeglé, L. Subtropical subsidence and surface deposition of oxidized mercury produced in the free troposphere. *Atmos. Chem. Phys.* **2017**, *17*, 8999−9017.
(20) Chen, X.; Balasubramanian, R.; Zhu, Q.; Behera, S. N.; Bo, D.; Huang, X.; Xie, H.; Cheng, J. Characteristics of atmospheric particulate mercury in size-fractionated particles during haze days in Shanghai. *Atmos. Environ.* **2016**, *131*, 400−408.
(21) Subir, M.; Ariya, P. A.; Dastoor, A. P. A review of the sources of uncertainties in atmospheric mercury modeling II. Mercury surface and heterogeneous chemistry−A missing link. *Atmos. Environ.* **2012**, *46*, 1−10.
(22) Edwards, P. M.; Brown, S. S.; Roberts, J. M.; Ahmadov, R.; Banta, R. M.; deGouw, J. A.; Dube, W. P.; Field, R. A.; Flynn, J. H.; Gilman, J. B.; Graus, M.; Helmig, D.; Koss, A.; Langford, A. O.; Lefer, B. L.; Lerner, B. M.; Li, R.; Li, S.-M.; McKeen, S. A.; Murphy, S. M.; Parrish, D. D.; Senff, C. J.; Soltis, J.; Stutz, J.; Sweeney, C.; Thompson, C. R.; Trainer, M. K.; Tsai, C.; Veres, P. R.; Washenfelder, R. A.; Warneke, C.; Wild, R. J.; Young, C. J.; Yuan, B.; Zamora, R. High winter ozone pollution from carbonyl photolysis in an oil and gas basin. *Nature* **2014**, *514*, 351−354.
(23) Lyman, S. N.; Gratz, L. E.; Dunham-Cheatham, S. M.; Gustin, M. S.; Luippold, A. Improvements to the accuracy of atmospheric oxidized mercury measurements. *Environ. Sci. Technol.* **2020**, *54*, 13379−13388.
(24) Lyman, S.; Tran, T. Inversion structure and winter ozone distribution in the Uintah Basin, Utah, USA. *Atmos. Environ.* **2015**, *123*, 156−165.
(25) Oltmans, S.; Schnell, R.; Johnson, B.; Pétron, G.; Mefford, T.; Neely, R., III Anatomy of wintertime ozone associated with oil and natural gas extraction activity in Wyoming and Utah. *Elementa* **2014**, *2*, No. 000024.
(26) Lareau, N. P.; Crosman, E.; Whiteman, C. D.; Horel, J. D.; Hoch, S. W.; Brown, W. O.; Horst, T. W. The persistent cold-air pool study. *Bull. Am. Meteorol. Soc.* **2013**, *94*, 51−63.
(27) Mansfield, M. L.; Lyman, S. N. Winter Ozone Pollution in Utah's Uinta Basin is Attenuating. *Atmosphere* **2021**, *12*, No. 4.
(28) Foster, C. S.; Crosman, E. T.; Horel, J.; Lyman, S.; Fasoli, B.; Bares, R.; Lin, J. Quantifying methane emissions in the Uintah Basin during wintertime stagnation episodes. *Elementa* **2019**, *7*, No. 24.
(29) Lyman, S. N.; Tran, T.; Mansfield, M. L.; Ravikumar, A. P. Aerial and ground-based optical gas imaging survey of Uinta Basin oil and gas wells. *Elementa* **2019**, *7*, No. 43.
(30) Tran, T.; Tran, H.; Mansfield, M.; Lyman, S.; Crosman, E. Four dimensional data assimilation (FDDA) impacts on WRF performance in simulating inversion layer structure and distributions of CMAQ-simulated winter ozone concentrations in Uintah Basin. *Atmos. Environ.* **2018**, *177*, 75−92.
(31) Mansfield, M. L. Statistical analysis of winter ozone exceedances in the Uintah Basin, Utah, USA. *J. Air Waste Manage. Assoc.* **2018**, *68*, 403−414.
(32) Matichuk, R.; Tonnesen, G.; Luecken, D.; Gilliam, R.; Napelenok, S. L.; Baker, K. R.; Schwede, D.; Murphy, B.; Helmig, D.; Lyman, S. N.; Roselle, S. Evaluation of the Community Multiscale Air Quality Model for Simulating Winter Ozone Formation in the Uinta Basin. *J. Geophys. Res.: Atmos.* **2017**, *122*, 13545−13572.
(33) Zatko, M.; Erbland, J.; Savarino, J.; Geng, L.; Easley, L.; Schauer, A.; Bates, T.; Quinn, P. K.; Light, B.; Morison, D.; Osthoff, H. D.; Lyman, S.; Neff, W.; Yuan, B.; Alexander, B. The magnitude of the snow-sourced reactive nitrogen flux to the boundary layer in the Uintah Basin, Utah, USA. *Atmos. Chem. Phys.* **2016**, *16*, 13837−13851.
(34) Wilkey, J.; Kelly, K.; Jaramillo, I. C.; Spinti, J.; Ring, T.; Hogue, M.; Pasqualini, D. Predicting emissions from oil and gas operations in the Uinta Basin, Utah. *J. Air Waste Manage. Assoc.* **2016**, *66*, 528−545.
(35) Neemann, E. M.; Crosman, E. T.; Horel, J. D.; Avey, L. Simulations of a cold-air pool associated with elevated wintertime ozone in the Uintah Basin, Utah. *Atmos. Chem. Phys.* **2015**, *15*, 135−151.
(36) Ahmadov, R.; McKeen, S.; Trainer, M.; Banta, R.; Brewer, A.; Brown, S.; Edwards, P. M.; de Gouw, J. A.; Frost, G. J.; Gilman, J.; Helmig, D.; Johnson, B.; Karion, A.; Koss, A.; Langford, A.; Lerner, B.; Olson, J.; Oltmans, S.; Peischl, J.; Petron, G.; Pichugina, Y.; Roberts, J. M.; Ryerson, T.; Schnell, R.; Senff, C.; Sweeney, C.; Thompson, C.; Veres, P. R.; Warneke, C.; Wild, R.; Williams, E. J.; Yuan, B.; Zamora, R. Understanding high wintertime ozone pollution events in an oil- and natural gas-producing region of the western US. *Atmos. Chem. Phys.* **2015**, *15*, 411−429.
(37) Koss, A. R.; de Gouw, J.; Warneke, C.; Gilman, J.; Lerner, B.; Graus, M.; Yuan, B.; Edwards, P.; Brown, S.; Wild, R.; Roberts, J. M.; Bates, T.; Quinn, P. K. Photochemical aging of volatile organic compounds associated with oil and natural gas extraction in the Uintah Basin, UT, during a wintertime ozone formation event. *Atmos. Chem. Phys.* **2015**, *15*, 5727−5741.
(38) Helmig, D.; Thompson, C. R.; Evans, J.; Boylan, P.; Hueber, J.; Park, J. H. Highly elevated atmospheric levels of volatile organic compounds in the Uintah Basin, Utah. *Environ. Sci. Technol.* **2014**, *48*, 4707−4715.
(39) Lee, L.; Wooldridge, P. J.; Gilman, J. B.; Warneke, C.; de Gouw, J.; Cohen, R. C. Low temperatures enhance organic nitrate formation: evidence from observations in the 2012 Uintah Basin Winter Ozone Study. *Atmos. Chem. Phys.* **2014**, *14*, 12441−12454.
(40) Warneke, C.; Geiger, F.; Edwards, P. M.; Dube, W.; Petron, G.; Kofler, J.; Zahn, A.; Brown, S. S.; Graus, M.; Gilman, J. B.; Lerner, B. M.; Peischl, J.; Ryerson, T. B.; de Gouw, J. A.; Roberts, J. M. Volatile organic compound emissions from the oil and natural gas industry in the Uintah Basin, Utah: oil and gas well pad emissions compared to ambient air composition. *Atmos. Chem. Phys.* **2014**, *14*, 10977−10988.
(41) Mansfield, M. L. Kerogen maturation data in the Uinta Basin, Utah, USA, constrain predictions of natural hydrocarbon seepage into the atmosphere. *J. Geophys. Res.: Atmos.* **2014**, *119*, 3460−3475.
(42) Oltmans, S. J.; Karion, A.; Schnell, R.; Pétron, G.; Sweeney, C.; Wolter, S.; Neff, D.; Montzka, S.; Miller, B.; Helmig, D.; et al. A high ozone episode in winter 2013 in the Uinta Basin oil and gas region characterized by aircraft measurements. *Atmos. Chem. Phys. Discuss.* **2014**, *14*, 20117−20157.
(43) Mansfield, M. L.; Hall, C. F. Statistical analysis of winter ozone events. *Air Qual., Atmos. Health* **2013**, *6*, 687−699.
(44) Karion, A.; Sweeney, C.; Petron, G.; Frost, G.; Hardesty, R. M.; Kofler, J.; Miller, B. R.; Newberger, T.; Wolter, S.; Banta, R.; Brewer, A.; Dlugokencky, E.; Lang, P.; Montzka, S. A.; Schnell, R.; Tans, P.; Trainer, M.; Zamora, R.; Conley, S. Methane emissions estimate from airborne measurements over a western United States natural gas field. *Geophys. Res. Lett.* **2013**, *40*, 4393−4397.
(45) Huang, J.; Miller, M. B.; Edgerton, E.; Gustin, M. S. Use of criteria pollutants, active and passive mercury sampling, and receptor modeling to understand the chemical forms of gaseous oxidized mercury in Florida. *Atmos. Chem. Phys. Discuss.* **2015**, *15*, 12069−12105.

https://doi.org/10.1021/acs.est.2c02224
Environ. Sci. Technol. 2022, 56, 11225−11235

(46) Huang, J.; Gustin, M. S. Uncertainties of Gaseous Oxidized Mercury Measurements Using KCl-Coated Denuders, Cation-Exchange Membranes, and Nylon Membranes: Humidity Influences. *Environ. Sci. Technol.* **2015**, *49*, 6102−6108.
(47) Miller, M. B.; Dunham-Cheatham, S. M.; Gustin, M. S.; Edwards, G. C. Evaluation of cation exchange membrane performance under exposure to high Hg0 and HgBr2 concentrations. *Atmos. Meas. Tech.* **2019**, *12*, 1207−1217.
(48) Luippold, A.; Gustin, M. S.; Dunham-Cheatham, S. M.; Zhang, L. Improvement of quantification and identification of atmospheric reactive mercury. *Atmos. Environ.* **2020**, *224*, No. 117307.
(49) Sexauer Gustin, M.; Pierce, A. M.; Huang, J.; Miller, M. B.; Holmes, H.; Loria-Salazar, S. M. Evidence for different reactive Hg sources and chemical compounds at adjacent valley and high elevation locations. *Environ. Sci. Technol.* **2016**, *50*, 12225−12231.
(50) Mao, N.; Khalizov, A. Exchange Reactions Alter Molecular Speciation of Gaseous Oxidized Mercury. *ACS Earth Space Chem.* **2021**, *5*, 1842−1853.
(51) Lyman, S. N.; Holmes, M.; Tran, H.; Tran, T.; O'Neil, T. High ethylene and propylene in an area dominated by oil production. *Atmosphere* **2021**, *12*, No. 1.
(52) Draxler, R. R.; Rolph, G. D. *HYSPLIT (HYbrid Single-Particle Lagrangian Integrated Trajectory) Model*; NOAA Air Resources Laboratory: Silver Spring, Maryland, 2003.
(53) Wolfe, G. M.; Marvin, M. R.; Roberts, S. J.; Travis, K. R.; Liao, J. The framework for 0-D atmospheric modeling (F0AM) v3.1. *Geosci. Model Dev.* **2016**, *9*, 3309−3319.
(54) NASA Giovanni: The Bridge between Data and Science. https://giovanni.gsfc.nasa.gov/giovanni/ (July 3, 2021).
(55) Stoeckenius, T.; McNally, D., Eds. *Final Report: 2013 Uinta Basin Winter Ozone Study*; Utah Division of Air Quality, March, 2014.
(56) Holmes, C. D.; Jacob, D. J.; Corbitt, E. S.; Mao, J.; Yang, X.; Talbot, R.; Slemr, F. Global atmospheric model for mercury including oxidation by bromine atoms. *Atmos. Chem. Phys.* **2010**, *10*, 12037−12057.
(57) Gratz, L. E.; Ambrose, J.; Jaffe, D.; Shah, V.; Jaeglé, L.; Stutz, J.; Festa, J.; Spolaor, M.; Tsai, C.; Selin, N.; Song, S.; Zhou, X.; Weinheimer, A.; Knapp, D. J.; Montzka, D. D.; Flocke, F.; Campos, T.; Apel, E. C.; Hornbrook, R. S.; Blake, N.; Hall, S.; Tyndall, G.; Reeves, M.; Stechman, D.; Stell, M. Oxidation of mercury by bromine in the subtropical Pacific free troposphere. *Geophys. Res. Lett.* **2015**, *42*, 10494−10502.
(58) Sherwen, T.; Schmidt, J. A.; Evans, M. J.; Carpenter, L. J.; Großmann, K.; Eastham, S. D.; Jacob, D. J.; Dix, B.; Koenig, T. K.; Sinreich, R.; Ortega, I.; Volkamer, R.; Saiz-Lopez, A.; Prados-Roman, C.; Mahajan, A. S.; Ordonez, C. Global impacts of tropospheric halogens (Cl, Br, I) on oxidants and composition in GEOS-Chem. *Atmos. Chem. Phys.* **2016**, *16*, 12239−12271.
(59) Saunders, S. M.; Jenkin, M. E.; Derwent, R.; Pilling, M. Protocol for the development of the Master Chemical Mechanism, MCM v3 (Part A): tropospheric degradation of non-aromatic volatile organic compounds. *Atmos. Chem. Phys.* **2003**, *3*, 161−180.
(60) Bloss, C.; Wagner, V.; Jenkin, M.; Volkamer, R.; Bloss, W.; Lee, J.; Heard, D.; Wirtz, K.; Martin-Reviejo, M.; Rea, G.; et al. Development of a detailed chemical mechanism (MCMv3. 1) for the atmospheric oxidation of aromatic hydrocarbons. *Atmos. Chem. Phys.* **2005**, *5*, 641−664.
(61) Pal, B.; Ariya, P. A. Studies of ozone initiated reactions of gaseous mercury: kinetics, product studies, and atmospheric implications. *Phys. Chem. Chem. Phys.* **2004**, *6*, 572−579.
(62) Zhang, L.; Brook, J.; Vet, R. A revised parameterization for gaseous dry deposition in air-quality models. *Atmos. Chem. Phys.* **2003**, *3*, 2067−2082.
(63) Lyman, S. N.; Gustin, M. S.; Prestbo, E. M.; Marsik, F. J. Estimation of Dry Deposition of Atmospheric Mercury in Nevada by Direct and Indirect Methods. *Environ. Sci. Technol.* **2007**, *41*, 1970−1976.
(64) Benjamin, S. G.; Weygandt, S. S.; Brown, J. M.; Hu, M.; Alexander, C. R.; Smirnova, T. G.; Olson, J. B.; James, E. P.; Dowell, D. C.; Grell, G. A.; et al. A North American hourly assimilation and model forecast cycle: The Rapid Refresh. *Mon. Weather Rev.* **2016**, *144*, 1669−1694.
(65) Streets, D. G.; Horowitz, H. M.; Lu, Z.; Levin, L.; Thackray, C. P.; Sunderland, E. M. Global and regional trends in mercury emissions and concentrations, 2010−2015. *Atmos. Environ.* **2019**, *201*, 417−427.
(66) Jaffe, D. Relationship between surface and free tropospheric ozone in the western US. *Environ. Sci. Technol.* **2011**, *45*, 432−438.
(67) Strode, S. A.; Rodriguez, J. M.; Logan, J. A.; Cooper, O. R.; Witte, J. C.; Lamsal, L. N.; Damon, M.; Van Aartsen, B.; Steenrod, S. D.; Strahan, S. E. Trends and variability in surface ozone over the United States. *J. Geophys. Res.* **2015**, *120*, 9020−9042.
(68) Lan, X.; Talbot, R.; Castro, M.; Perry, K.; Luke, W. Seasonal and diurnal variations of atmospheric mercury across the US determined from AMNet monitoring data. *Atmos. Chem. Phys.* **2012**, *12*, 10569−10582.
(69) Zhou, H.; Zhou, C.; Hopke, P. K.; Holsen, T. M. Mercury wet deposition and speciated mercury air concentrations at rural and urban sites across New York state: Temporal patterns, sources and scavenging coefficients. *Sci. Total Environ.* **2018**, *637−638*, 943−953.
(70) Liu, B.; Keeler, G. J.; Dvonch, J. T.; Barres, J. A.; Lynam, M. M.; Marsik, F. J.; Morgan, J. T. Urban−rural differences in atmospheric mercury speciation. *Atmos. Environ.* **2010**, *44*, 2013−2023.
(71) Lynam, M. M.; Keeler, G. J. Automated speciated mercury measurements in Michigan. *Environ. Sci. Technol.* **2005**, *39*, 9253−9262.
(72) Swartzendruber, P. C.; Jaffe, D. A.; Prestbo, E. M.; Weiss-Penzias, P.; Selin, N. E.; Park, R.; Jacob, D. J.; Strode, S.; Jaeglé, L. Observations of reactive gaseous mercury in the free troposphere at the Mt. Bachelor Observatory. *J. Geophys. Res.: Atmos.* **2006**, *111*, No. D24301.
(73) Kumar, R.; Naja, M.; Pfister, G.; Barth, M.; Brasseur, G. P. Source attribution of carbon monoxide in India and surrounding regions during wintertime. *J. Geophys. Res.: Atmos.* **2013**, *118*, 1981−1995.
(74) Calvert, J. G.; Lindberg, S. E. Mechanisms of mercury removal by O3 and OH in the atmosphere. *Atmos. Environ.* **2005**, *39*, 3355−3367.
(75) Lyman, S. N.; Jaffe, D. A. Elemental and oxidized mercury in the upper troposphere and lower stratosphere. *Nat. Geosci.* **2012**, *5*, 114−117.
(76) Gustin, M. S.; Huang, J.; Miller, M. B.; Peterson, C.; Jaffe, D. A.; Ambrose, J.; Finley, B. D.; Lyman, S. N.; Call, K.; Talbot, R.; Feddersen, D.; Mao, H.; Lindberg, S. Do we understand what the mercury speciation instruments are actually measuring? Results of RAMIX. *Environ. Sci. Technol.* **2013**, *47*, 7295−7306.
(77) Ambrose, J. L.; Gratz, L. E.; Jaffe, D. A.; Campos, T.; Flocke, F. M.; Knapp, D. J.; Stechman, D. M.; Stell, M.; Weinheimer, A. J.; Cantrell, C. A.; Mauldin, R. L. Mercury emission ratios from coal-fired power plants in the Southeastern United States during NOMADSS. *Environ. Sci. Technol.* **2015**, *49*, 10389−10397.
(78) Luippold, A.; Gustin, M. S.; Dunham-Cheatham, S. M.; Castro, M.; Luke, W.; Lyman, S.; Zhang, L. Use of multiple lines of evidence to understand reactive mercury concentrations and chemistry in Hawai'i, Nevada, Maryland, and Utah, USA. *Environ. Sci. Technol.* **2020**, *54*, 7922−7931.
(79) Peleg, M.; Tas, E.; Matveev, V.; Obrist, D.; Moore, C. W.; Gabay, M.; Luria, M. Observational evidence for involvement of nitrate radicals in nighttime oxidation of mercury. *Environ. Sci. Technol.* **2015**, *49*, 14008−14018.
(80) Dibble, T. S.; Zelie, M.; Mao, H. Thermodynamics of reactions of ClHg and BrHg radicals with atmospherically abundant free radicals. *Atmos. Chem. Phys.* **2012**, *12*, 10271−10279.
(81) Hynes, A. J.; Donohoue, D. L.; Goodsite, M. E.; Hedgecock, I. M. Our Current Understanding of Major Chemical and Physical Processes Affecting Mercury Dynamics in the Atmosphere and at the Air-Water/Terrestrial Interfaces. In *Mercury Fate and Transport in the Global Atmosphere*; Mason, R.; Pirrone, N., Eds.; Springer, 2009; pp 427−457.

(82) Peng, X.; Wang, W.; Xia, M.; Chen, H.; Ravishankara, A. R.; Li, Q.; Saiz-Lopez, A.; Liu, P.; Zhang, F.; Zhang, C.; et al. An unexpected large continental source of reactive bromine and chlorine with significant impact on wintertime air quality. *Natl. Sci. Rev.* **2021**, *8*, No. nwaa304.
(83) Gabay, M.; Raveh-Rubin, S.; Peleg, M.; Fredj, E.; Tas, E. Is oxidation of atmospheric mercury controlled by different mechanisms in the polluted continental boundary layer vs. remote marine boundary layer? *Environ. Res. Lett.* **2020**, *15*, No. 064026.
(84) Lyman, S. N. *Elemental and Oxidized Mercury in the Atmosphere at Horsepool, Utah, January−July 2019*. Utah State University Digital Commons; Utah State University: Logan, Utah, 2022.

https://doi.org/10.1021/acs.est.2c02224
Environ. Sci. Technol. 2022, 56, 11225−11235